Poiseuille flow over a wavy surface

Poisseuille flow over a wavy surface

Simon J Haward and Amy Q Shen
Okinawa Institute of Science and Technology Graduate University
1919-1 Tancha, Onna-son, Okinawa 904-0495, Japan

Jacob Page
School of Mathematics, University of Bristol, Bristol BS8 1TW, UK

Tamer A. Zaki
Department of Mechanical Engineering, Johns Hopkins University, Baltimore, MD 21218, USA
(Dated: April 2017; Revised July 26, 2017)

We present a detailed series of experiments using spatially-resolved flow velocimetry to examine the flow of Newtonian fluids through rectangular channels with one wavy surface of wavenumber k. The glass channels are fabricated by the novel method of selective laser-induced etching, which allows them to be made with a high (quasi-2D) aspect ratio (width/depth, $w/2d = 5$) and with an accurate wave profile of small relative amplitude ($A/d = 0.05$, $A < k$). Following the prior theoretical work for plane Couette flow over a wavy surface [F. C. Charru and E. J. Hinch, "'Phase diagram' of interfacial instabilities in a two-layer Couette flow and mechanism of the long-wave instability," J. Fluid Mech. **414**, 195-223 (2000)], we examine the influence of two dimensionless parameters (the normalized channel depth $\alpha = kd$ and the viscous length scale θ) on the penetration depth $\mathcal{P}$ of the perturbations that the wavy surface induces to the Poisseuille base flow. The asymptotic analysis by Charru and Hinch predicted three regimes of behavior classified as 'shallow viscous' ($\mathcal{P} \approx \alpha$), 'deep viscous' ($\mathcal{P} \approx \pi$), and 'inviscid' ($\mathcal{P} \sim \theta$). All three regimes are here verified experimentally. Minor differences in details of the 'phase diagrams' for the flow regimes in $\alpha - \theta$ parameter space observed between Poisseuille and plane Couette flow are attributed to the contrasting boundary conditions in the different flow configurations. The experimental results presented here also compare favorably to results from linear theory for a Poiseuille base flow, and thus establish a detailed experimental complement to the theory.

I. INTRODUCTION

In this work we experimentally examine the Poisseuille flow of Newtonian fluids through rectangular channels with a small amplitude sinusoidal perturbation applied to the surface of one of the channel walls. The problem is a relevant model for understanding the effects of channel wall roughness and can also be considered as a model for the action of shearing between unstable interfaces in multi-layer flows [1–4]. The problem is also relevant to shear-induced deformations of soft walls at moderate Reynolds numbers in microchannels [5, 6], while at higher Reynolds numbers such studies lend insight into the formation and motion of subaqueous ripples in coastal areas and river beds, and of sand dunes in the desert [7, 8].

Here we use spatially-resolved micro-particle image velocimetry (μ-PIV) to characterize perturbations to the Poisseuille base flow state that are induced by the presence of the wavy wall. The wave has an amplitude $A \ll d$ and $A \ll \lambda$, where d is the channel half-depth, and λ is the wavelength of the surface. We vary λ relative to d in order to span the 'deep' ($2\pi d/\lambda \gtrsim 1$) and 'shallow' ($2\pi d/\lambda \lesssim 1$) regimes, see schematic diagram in Fig. 1 [2, 4]. We restrict our study to the viscous and inertial (or inviscid) laminar regimes and we analyze our data in the context of the 'phase diagram' proposed by Charru and Hinch [2] for plane Couette flow over a wavy surface. It might be expected *a-priori* that, when viscous effects are dominant and the shear rate is unimportant, the two configurations (Couette and Poisseuille) should recover similar behavior [2]. However, when the viscous and inertial timescales are commensurate, the different mean-shear distributions in the two configuarations is more likely to have an effect on the phase diagram. The experimental establishment of these basic flow regimes in the phase diagram for Poisseuille flow over wavy surfaces will provide a benchmark for future experimental stud-

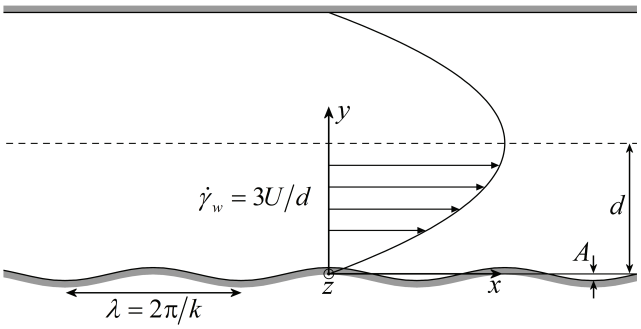

FIG. 1. Poisseuille flow through a channel with a wavy bottom surface. The channel has a half-depth d, while the wavy surface has wavelength λ and amplitude $A \ll d$. The wall shear rate $\dot{\gamma}_w = 3U/d$, where U is the average flow velocity through the channel. The spanwise direction (through z) is out of the page.

ies that consider more complex geometrical arrangements and flows. Possible examples include studies of localized wall roughness, flow unsteadiness, and the effects of non-Newtonian fluid rheology. The latter example is of interest across a wide range of Reynolds numbers, from the inertialess to the inertio-elastic regimes [4]. We note that, while there are a large number of studies of flows through pipes and channels with undulating walls, these typically involve large variations in flow cross-section, which can be relevant to processes such as peristaltic pumping [9] and biophysical applications [10]. There are no previous experimental studies in the literature that examine steady laminar flows through channels in which the periodic boundary essentially serves as a perturbation to the base shear flow.

II. PROBLEM DESCRIPTION

Fig. 1 shows a schematic representation of the problem under consideration. We consider channels of average half-depth d with a sinusoidal wave of wavelength λ (wavenumber $k = 2\pi/\lambda$) and amplitude A on the bottom wall. The spanwise width w of the channel (through z) is assumed $\gg d$ to provide an approximation to two-dimensional (2D) flow, and the amplitude A is assumed $\ll d$ and $\ll \lambda$ in order to conform to the linear perturbation assumption [2, 4]. In this work, we employ Poisseuille flow rather than plane Couette flow (as used in prior linear analyses [2, 4]) simply for the considerable experimental convenience offered by the former. Here, our focus is placed on the flow domain defined by the region of monotonically increasing flow velocity between the wavy surface and the channel centreline ($0 < y < d$).

As a characteristic shear rate in the channel we take the wall value for Poisseuille flow in a channel of half-depth d:

$$\dot{\gamma}_w = \frac{3U}{d}, \tag{1}$$

where the average flow velocity $U = Q/2dw$ and Q is the imposed volumetric flow rate.

The Reynolds number of the flow is defined as:

$$Re = \frac{2\rho U d}{\eta}, \tag{2}$$

where η is the dynamic viscosity of the Newtonian fluid.

According to Charru and Hinch [2], we classify the flow in the wavy channels according to two additional dimensionless parameters: (1) the normalized channel depth:

$$\alpha = kd = \frac{2\pi d}{\lambda}, \tag{3}$$

and (2) the normalized viscous length scale:

$$\theta = \left(\frac{\eta k^2}{\rho \dot{\gamma}_w}\right)^{1/3} = \left(\frac{2\alpha^2}{3Re}\right)^{1/3}. \tag{4}$$

In plane Couette flow over wavy surfaces, Charru and Hinch classified channels for which $\alpha \gtrsim 1$ as 'deep' and channels for which $\alpha \lesssim 1$ as 'shallow' [2]. Three broad regimes of flow were identified: (i) a shallow viscous regime with $\alpha \lesssim 1$ and $\theta > \alpha$ in which the channel depth is less than the viscous length and vorticity perturbations penetrate through the entire channel; (ii) a deep viscous regime with $\alpha \gtrsim 1$ and $\theta \gtrsim 1$ in which vorticity perturbations are unaffected by either boundary or flow conditions and penetrate approximately one wavelength into the channel; (iii) an inviscid regime with $\alpha \gtrsim \theta$ and $\theta \lesssim 1$, in which the perturbation is influenced by inertia and the depth of the vorticity penetration scales with θ. Here we will test experimentally whether the same pair of parameters describe a similar set of regimes for Poiseuille flow over wavy surfaces.

III. EXPERIMENTAL METHODS

We employ five fluidic devices, which all share common dimensions with the exception of the wavelength of the surface roughness present in a section of one of the channel walls. Fig. 2 shows optical micrographs of the five channels used in the study, and for convenience Table I lists the relevant dimensions of each of the five geometries. The devices are fabricated in fused silica using the LightFab 3D printer (Lightfab, GmbH), which employs the technique of selective laser-induced etching (SLE) [11]. This technique allows the fabrication of devices with a high aspect ratio, an accurate wave profile (± 1 μm precision) and that are resistant to channel deformation at even very high imposed flow rates or pressures. The channels all have a half-depth of $d = 200$ μm and a span through the z-direction of $w = 2$ mm. This provides an aspect ratio $AR = w/2d = 5$ and hence a reasonable approximation to 2D flow near the channel midplane, $z = w/2$. The wavy surface located at $y = 0$ (see Fig. 1) has amplitude $A = 10$ μm (i.e. $A/d = 0.05$), such that the ratio of maximum to minimum channel cross-sectional area is given by $CR = 410/390 \approx 1.05$. The wavelength of the rough surface is varied in the range $0.125 \leq \lambda \leq 2$ mm, thus providing normalized channel depths in the range $0.2\pi \leq \alpha \leq 3.2\pi$ while maintaining $A \leq 0.08\lambda$, see Table I. An upstream section of parallel channel of depth $2d$, span w and length $L = 10$ mm is incorporated in order to allow the flow to become fully-developed prior to reaching the downstream wavy wall. The wavy section itself is also 10 mm in length, and thus incorporates a minimum of five complete waves in the case of Device 1 ($\lambda = 2$ mm), and more waves for the other four devices with shorter wavelengths (see Table I). To the left hand side of the photographs provided in Fig. 2, a short section of the upstream parallel region of the channel is evident immediately before the start of the wavy region to the right.

Flow through the devices is driven along the x-direction using a high-precision neMESYS low pressure

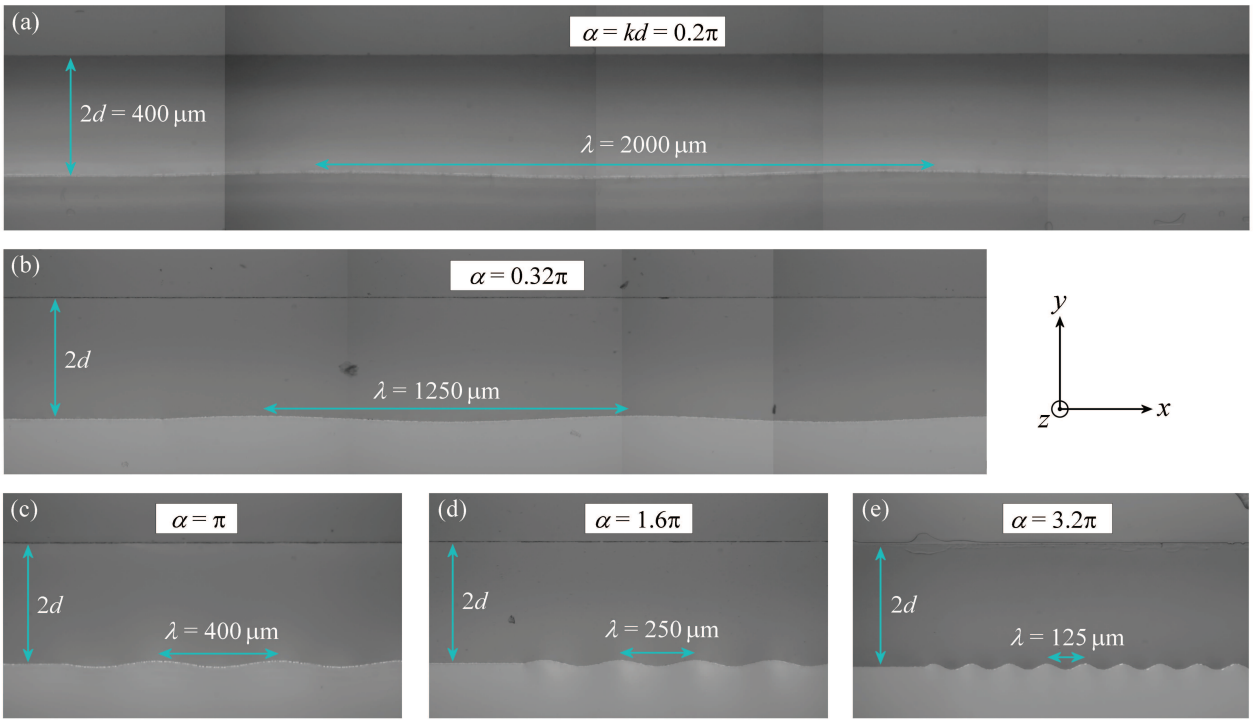

FIG. 2. Photographs of the five wavy-walled microchannels used in the flow experiments. All the devices have half-depth $d = 200$ μm, wave amplitude $A = 10$ μm, and a spanwise width height $w = 2$ mm through the z-direction (out of the page). The channels differ only in the respective wavelength of their wavy surfaces: (a) $\lambda = 2000$ μm, $\alpha = 0.2\pi$, (b) $\lambda = 1250$ μm, $\alpha = 0.32\pi$, (c) $\lambda = 400$ μm, $\alpha = \pi$, (d) $\lambda = 250$ μm, $\alpha = 1.6\pi$, (e) $\lambda = 125$ μm, $\alpha = 3.2\pi$.

TABLE I. Salient dimensions of the wavy-walled channels

Device	d [mm]	h [mm]	A [μm]	λ [mm]	k [mm^{-1}]	α
1	0.2	2	10	2.0	π	0.2π
2	0.2	2	10	1.25	1.6π	0.32π
3	0.2	2	10	0.4	5π	π
4	0.2	2	10	0.25	8π	1.6π
5	0.2	2	10	0.125	16π	3.2π

syringe pump (Cetoni, GmbH) fitted with a Hamilton Gastight glass syringe connected to the device via silicone tubing. Two Newtonian fluids of different viscosities are used in order to access the different regimes of flow (viscous and inviscid). One of the fluids is plain deionized (DI) water, and the second fluid is DI water viscosified by the addition of 13 wt% poly(ethylene glycol) (8000 g mol^{-1}, Sigma-Aldrich). The viscosities of the fluids have been measured at 25°C using a DHR3 stress-controlled rheometer (TA Instruments, Inc) fitted with a 40 mm diameter 1° cone-plate fixture, yielding $\eta = 0.87$ mPa s and $\eta = 7.72$ mPa s for the DI water and 13 wt% aqueous PEG, respectively. The densities of the fluids have been measured at 25°C by weighing of fluid dispensed from calibrated micro-pipettes, yielding values of $\rho = 996.9$ kg m^{-3} and $\rho = 1015.5$ kg m^{-3} for the DI water and the 13 wt% aqueous PEG, respectively. The values of η and ρ obtained for the 13 wt% aqueous PEG are in line with expectations based on previous reports in the literature [12, 13].

Measurements of flow velocity vector fields within the wavy channels are made using a micro-particle image velocimetry (μ-PIV) system (TSI, Inc). For this purpose fluids are seeded with 1 μm diameter fluorescent microparticles (nile red FluoSpheres, Life Technologies) with excitation and emission wavelengths of 535 and 575 nm, respectively. The flow channel is placed on the imaging stage of an inverted microscope (Nikon Eclipse Ti) and the mid-plane of the device ($z = w/2$) is brought into focus. The fluid is illuminated through the microscope objective by a dual-pulsed Nd:YLF laser at 527 nm, which excites the fluorescent particles. The light emitted by the particles is imaged through the same objective lens, passed through an epifluorescent filter in order to eliminate the background laser light and projected onto the sensor array of a high speed Phantom Miro camera (Vision Research, Inc), operating in frame-straddling mode. Images are captured in pairs in synchronicity with the pairs of laser pulses. The time between laser pulses Δt is set such that the average particle displacement between images in the corresponding image pair is around 8 pixels, which is optimal for the cross-correlation PIV algorithm used to obtain velocity vectors based on a 32×32

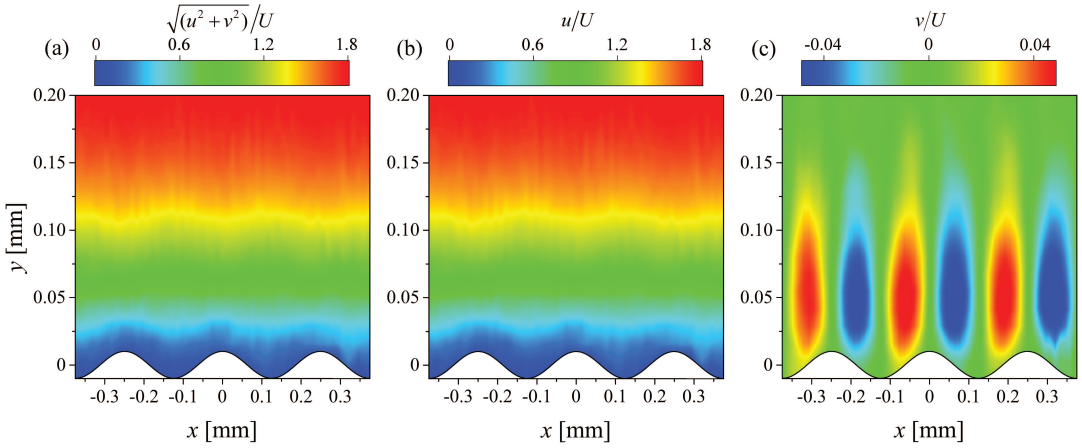

FIG. 3. Typical example of a flow field obtained in Device 4 ($\lambda = 0.25$ mm, $\alpha = 1.6\pi$) for the flow of 13 wt% PEG at a flow rate of $Q = 1.78$ mL min^{-1} ($U = 37.1$ mm s^{-1}, $\dot{\gamma}_w = 556.25$ s^{-1}, $Re = 1.95$, $\theta = 2.05$). (a) Normalized velocity magnitude field, (b) Normalized x-velocity component, u/U. (c) Normalized y-velocity component, v/U. Flow is from left to right.

pixel grid. For each flow rate examined in each device, vector fields are ensemble-averaged over the data from 20 image pairs. Due to the various wavelengths of the devices, a range of objective lenses are used in the experiments in order to provide the maximum possible spatial resolution while also allowing at least one full wave of the rough surface to be visualized in each case. For Devices 1 and 2, a 4× NA = 0.13 objective is used; for Device 3 a 5× NA = 0.15 objective is used, and for Devices 4 and 5 a 10× NA = 0.3 objective is used. The corresponding measurement width, over which microparticles contribute to the determination of velocity vectors, is $\delta z_m \approx 142$, 109 and 31 μm for the 4×, 5× and 10× lenses, respectively [14]. Even in the worst case of the 4× objective lens, δz_m is only 7% of the channel width, so should not result in any significant measurement error given the high channel aspect ratios and therefore the expected 2D nature of the flow close to the mid-plane.

An example of a typical velocity field measurement (in this case coming from Device 4, with $\lambda = 0.25$ mm and an imposed average flow velocity of $U = 37.1$ mm s^{-1} with the 13 wt% aqueous PEG solution) is shown in Fig. 3. Such conditions correspond to $\alpha = 1.6\pi$, $\theta = 2.05$ and hence are expected to fall into the deep viscous regime ($\alpha \gtrsim 1$, $\theta \gtrsim 1$) [2]. Fig. 3a shows the normalized velocity magnitude field $\sqrt{(u^2+v^2)}/U$ (where u and v are the x and y velocity components, respectively), imaged over three wavelengths of the wavy surface. Fig. 3b shows the normalized field of x velocity component, u/U. There is an almost imperceptible difference between Figs. 3a and 3b, which clearly shows the flow field is dominated by u. In Fig. 3c, we show the normalized y-component of the velocity field, v/U. Here, the effect of the wavy surface is clearly apparent, with positive v values measured above rising edges of the wave and negative v values measured above falling surfaces of the wave. However, it is worthwhile mentioning the magnitude of v is quite small ($\sim O(0.05U)$). Such small velocity components can be quite challenging to measure by μ-PIV and also demonstrate the small perturbation caused by the wavy surface to the Poisseuille base flow. Since for a Poisseuille flow $v_{\mathrm{Pois}} \equiv 0$, our measurement of v allows a simple and direct determination of the perturbation component $v' = v - v_{Pois} \equiv v$.

In this work, we use this v' perturbation component to evaluate an experimental measure of the penetration depth $\mathcal{P}_v$ of the disturbance by using a criterion similar to that employed by Page and Zaki [4]:

$$\mathcal{P}_v \equiv ky(\Lambda_v = 0.95), \text{ where } \Lambda_v(y) = \frac{\int_0^y |v'(y)|^2 dy}{\int_0^d |v'(y)|^2 dy}. \quad (5)$$

For each value of y, we evaluate $|v'(y)|$ by averaging v' over the full range of x in the field of view of the μ-PIV measurement. We have chosen to relax the criterion from $\Lambda = 0.99$ (used by Page and Zaki [4]) to $\Lambda_v = 0.95$ due to the additional noise present in our experimental data compared with their computations. We use a criterion similar to that suggested by Page and Zaki, as opposed to that used by Charru and Hinch [2], mainly because the criterion developed by Page and Zaki can account for any non-local vorticity away from the wavy channel wall [4]. Non-local vorticity amplification has recently been predicted for viscoelastic flow through wavy channels and we intend to investigate this phenomenon experimentally in future work, against which we wish to compare both our current results and the results of their linear theory.

Although various possible approaches can be conceived to extract a x-velocity perturbation component u' from our experimental data and thus to compute the full spanwise vorticity perturbation $\omega_z{}' = \partial v'/\partial x - \partial u'/\partial y$, we deliberately choose not to do this. We consider it a safer and more reliable approach to simply use v' to quantify

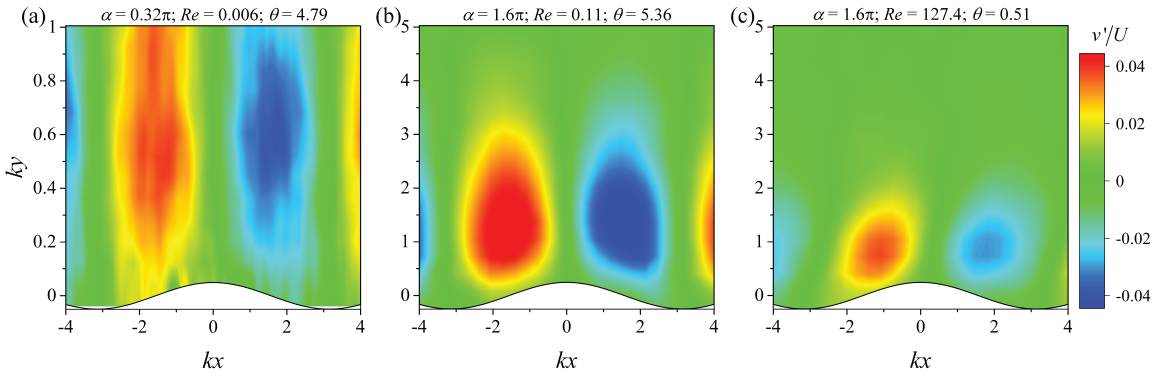

FIG. 4. Experimentally measured normalized fields of v' showing the y-velocity perturbations in the three regimes of flow. (a) 'Shallow viscous' regime ($\alpha < \pi$, $\theta > \alpha$) in Device 2 ($\alpha = 0.32\pi$). (b) 'Deep viscous' regime ($\alpha > \pi$, $\theta > 1$) in Device 4 ($\alpha = 1.6\pi$). (c) 'Inviscid' regime ($\alpha > \theta$, $\theta < 1$) in Device 4 ($\alpha = 3.2\pi$). Flow is from left to right.

the perturbation, as per Eq. 5. As will be shown, the v' perturbation component alone is sufficient to properly characterize the disturbance and has the advantage that it can be extracted directly from the measured velocity field without the need for any assumptions or approximations. Furthermore, we validate our experimental results against the linearized perturbation equations from which both u' and v' are available and thus allows the perturbation to be characterized according to both v' and ${\omega_z}'$, as explained next.

IV. LINEAR PERTURBATION EQUATIONS

The amplitude of the surface waviness over the range of α considered here is sufficiently low that linear theory can be invoked to explain the structure of the flow perturbations. In the linear limit, the wavy lower surface can be treated as a regular perturbation to smooth-walled Poiseuille flow, $\mathbf{U} \approx U_{\text{Pois.}}(y)\mathbf{e}_x + \mathbf{u}'(\mathbf{x})$, where $|\mathbf{u}'| \sim \epsilon U$. The amplitude of the small perturbation, $\epsilon \ll 1$, is arbitrary in the linear problem. Here we use the amplitude of the wall roughness to define ϵ, which enables a direct quantitative comparison with the experimental results.

We adopt the disturbance ansatz $\mathbf{u}'(\mathbf{x}) = \Re\left[\hat{\mathbf{u}}(y)\exp(ikx)\right]$. The (dimensional) linear equations for $\hat{\mathbf{u}}$ are

$$ik\hat{u} + \frac{d\hat{v}}{dy} = 0, \tag{6a}$$

$$ik\overline{U}\hat{u} + \overline{U}'\hat{v} = -ik\frac{\hat{p}}{\rho} + \nu\left(\frac{d^2}{dy^2} - k^2\right)\hat{u}, \tag{6b}$$

$$ik\overline{U}\hat{v} = -\frac{1}{\rho}\frac{d\hat{p}}{dy} + \nu\left(\frac{d^2}{dy^2} - k^2\right)\hat{v}, \tag{6c}$$

where $\overline{U}(y) = U_{\text{Pois.}}(y) = (3/2)U[1 - (y-d)^2/d^2]$. The total velocity vanishes on the wavy surface. Upon linearization, this requirement yields a homogenous boundary condition for the normal velocity, $\hat{v}(y=0) = 0$, and a slip condition on the streamwise velocity, $\hat{u}(y=0) = -\dot{\gamma}_w A$. Both velocity components vanish at the top wall. Note that the slip condition at the lower wall fixes the amplitude of the perturbation velocity, $\epsilon = 3A/d$.

Equations 6(a-c) are solved using an expansion in Chebyshev polynomials in the wall-normal coordinate, evaluated at the Gauss-Lobatto points. A total of $N = 100$ polynomials are used to accurately resolve the perturbation field.

From the results of the linear analysis, in addition to evaluating the penetration depth $\mathcal{P}_v$ according to Eq. 5, we also evaluate a similar quantity $\mathcal{P}_\omega$ by replacing v' in Eq. 5 with the full vorticity perturbation ${\omega_z}' = \partial v'/\partial x - \partial u'/\partial y$:

$$\mathcal{P}_\omega \equiv ky(\Lambda_\omega = 0.95),$$
$$\text{where } \Lambda_\omega(y) = \frac{\int_0^y |{\omega_z}'(y)|^2 dy}{\int_0^d |{\omega_z}'(y)|^2 dy}, \tag{7}$$

which is the same as the measure employed previously by Page and Zaki [4].

V. RESULTS

In our experiments in quasi-2D channel flow over wavy surfaces, we indeed observe three regimes of flow broadly comparable with those described by Charru and Hinch [2] and Page and Zaki [4] for plane Couette flow over a wavy surface. In Fig. 4, we show examples of the y-velocity perturbations v' caused by the Poisseuille flow over the wavy surface in each of the three regimes. In our case, as we will show, the shallow viscous regime occurs in channels with $\alpha < \pi$ and $\theta > \alpha$, as shown in Fig. 4a for the case of Device 2 ($\alpha = 0.32\pi$). Here, the perturbation is antisymmetric about $x = 0$, extends straight out from the wavy surface and penetrates all the way through the channel depth. For $\alpha > \pi$, the channel becomes deep. In the deep

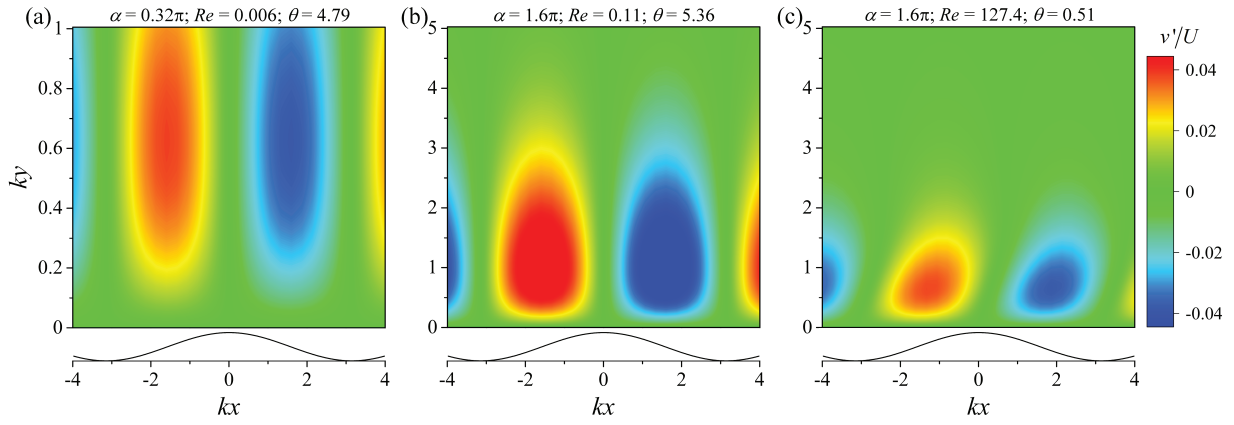

FIG. 5. Results from the linear equations for direct comparison with the experiments from Fig. 4. Normalized fields of v' for the cases: (a) 'Shallow viscous' regime with $\alpha = 0.32\pi$, $\theta = 4.79$. (b) 'Deep viscous' regime with $\alpha = 1.6\pi$, $\theta = 5.36$. (c) 'Inviscid' regime with $\alpha = 1.6\pi$, $\theta = 0.51$.

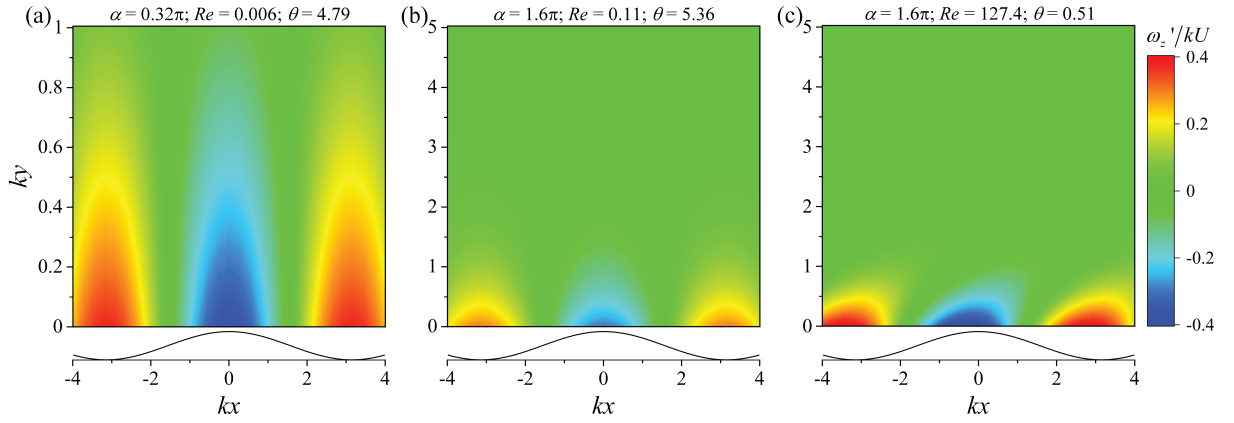

FIG. 6. Results from the linear equations for direct comparison with the experiments from Fig. 4 and the linear results shown in Fig. 5. Normalized fields of $\omega_z{}'$ for the cases: (a) 'Shallow viscous' regime with $\alpha = 0.32\pi$, $\theta = 4.79$. (b) 'Deep viscous' regime with $\alpha = 1.6\pi$, $\theta = 5.36$. (c) 'Inviscid' regime with $\alpha = 1.6\pi$, $\theta = 0.51$.

viscous regime (e.g. $\alpha = 1.6\pi$, $\theta \gtrsim 1$, Fig. 4b, for Device 4) the perturbation is again antisymmetric about $x = 0$ and extends straight out from the wavy surface. However, in this case the perturbation decays within the flow domain reaching a depth of $ky \approx \pi$ into the channel. The inviscid regime ($\alpha > \theta$, $\theta \lesssim 1$) is illustrated in Fig. 4c, here again for the channel with $\alpha = 1.6\pi$ (Device 4). Under this regime, inertia becomes significant and tilts the perturbation forwards. The perturbation becomes localized closer to the wavy surface, and the magnitude of the perturbation decreases noticeably compared with the deep viscous regime (Fig. 4b).

Fig. 5a-c present numerical results from linear theory. The v' perturbation fields are obtained under the same conditions as Fig. 4a-c, respectively. Note that the waviness of the bottom boundary is modeled in linear theory by a slip condition at the mean-wall location. As such, the bottom boundary is flat in Fig. 5. As can be seen, the qualitative comparison between the experiments (Fig. 4) and the linear theory (Fig. 5) is very favorable. The penetration of v' into the channel is progressively reduced, and the perturbation field is titled forward in the inviscid regime Fig. 5c.

The results from linear theory for $\omega_z{}'$ perturbation fields are presented in Fig. 6a-c. These again are obtained under the same geometric and flow conditions as the images in Figs. 4 and 5 parts a-c, respectively. Unlike the transverse velocity v', which peaks away from the wall, the peak in $\omega_z{}'$ is at the wavy surface, which is the site of vorticity injection. The perturbation then decays monotonically with increasing distance into the channel. The decay is within a smaller distance from the wall as compared with v' since the latter also includes an irrotational component.

Fig. 7 shows how the penetration depth of the perturbation depends on the imposed flow conditions within each of the five wavy channel devices. Fig. 7a presents $\mathcal{P}_v$ as a function of θ, determined from experimental mea-

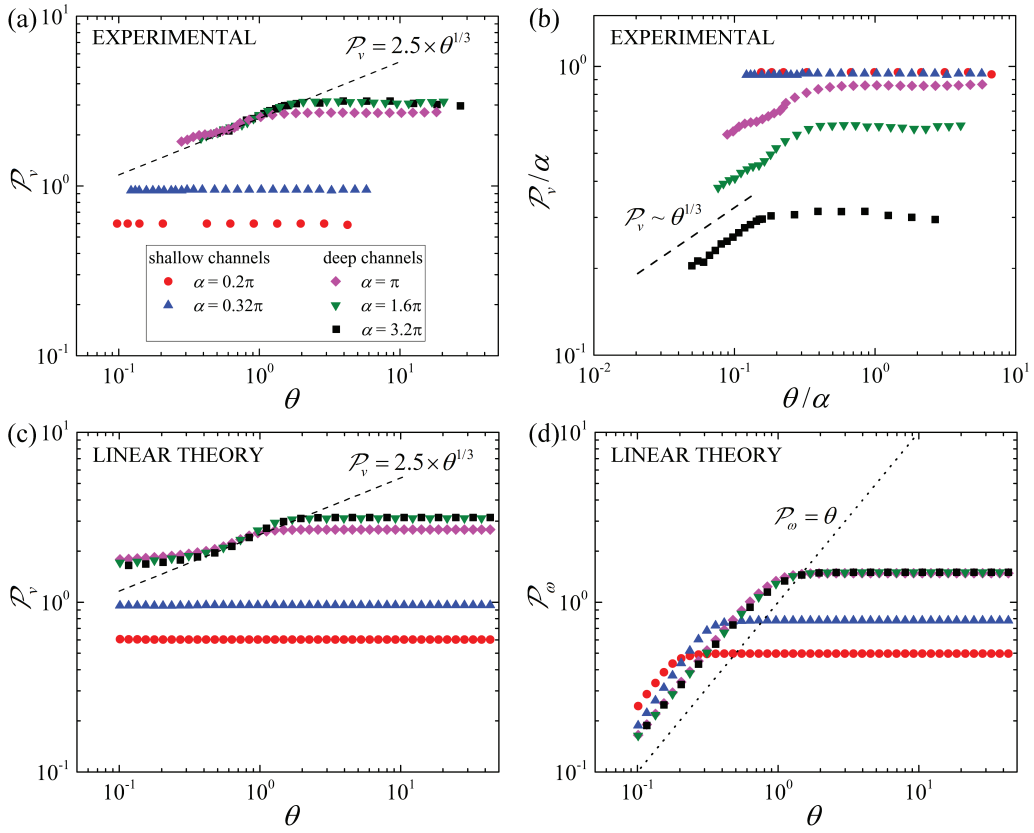

FIG. 7. (a) Experimental penetration depth $\mathcal{P}_v$ as a function of θ, and (b) normalized experimental penetration depth $\mathcal{P}_v/\alpha$ as a function of θ/α for each of the five wavy channel devices. Numerical penetration depth results from linear theory for (c) $\mathcal{P}_v$ as a function of θ, and (d) $\mathcal{P}_\omega$ as a function of θ.

surements. Here we can see that within shallow channels ($\alpha < \pi$), $\mathcal{P}_v \approx \alpha$ for the entire range of θ accessible in our experiment. In deep channels ($\alpha \geq \pi$), a plateau region of constant $\mathcal{P}_v$ for $\theta \gtrsim 1$ indicates the deep viscous regime. As the channel depth increases from shallow to deep, the plateau penetration depth $\mathcal{P}_v \to \pi$. An asymptotic regime appears to have been reached at $\alpha = 1.6\pi$ (≈ 5), as was shown theoretically for flow in a wavy plane Couette [2]. Here, $\mathcal{P}_v \approx \pi$ in the high-θ plateau. At lower $\theta \lesssim 1$, the inviscid regime in the deep channels is characterized by power-law behaviour with $\mathcal{P}_v \sim \theta^{1/3}$. Power-law behaviour was also shown by Charru and Hinch in the inviscid regime, but with a stronger θ dependence $\mathcal{P} \sim \theta$.

Fig. 7b, presents the experimental data in the form of $\mathcal{P}_v/\alpha$ as a function of θ/α. Here it is clear that as α decreases $\mathcal{P}_v \to \alpha$, reaching asymptotic behavior at $\alpha = 0.32\pi$ (≈ 1), as was also shown for flow in the wavy plane Couette [2]. Also from Fig. 7b, the onset of inviscid behavior is observed (in deep channels) for $\theta < \alpha$, as predicted.

Figs. 7c,d show the results of the penetration depth determined from linear theory for Poiseuille flow. Fig. 7c shows $\mathcal{P}_v$ as a function of θ, and is directly comparable to Fig. 7a, showing remarkably good agreement between the experiment and the simulation when this measure of penetration is used. This encouraging result lends validity to the experimental approach and demonstrates that the experimental flow channels conform well to the constraints of the linear assumption made in the theoretical model. Finally, Fig. 7d shows the result of using the full vorticity perturbation $\omega_z{}'$ to determine the penetration depth according to Eq. 7. Here, the expected scaling of $\mathcal{P} \sim \theta$ is recovered in the inviscid regime.

In general, the observations made in Fig. 7 are consistent with the earlier predictions for flow in the wavy plane Couette [2]. Differences between asymptotic values of $\mathcal{P}$ in deep channels, and $\mathcal{P}/\alpha$ in shallow channels, can be attributed to the contrasting boundary condition at $y = d$ ($ky = \alpha$). In the plane Couette there is a rigid no-slip boundary at $y = d$ through which the perturbation cannot penetrate. In the Poisseuille flow considered here, there is no physical boundary at $y = d$ and the perturbation is able to penetrate beyond the channel half-depth. Experimentally, we do not obtain the expected scaling for $\mathcal{P} \sim \theta$ in the inviscid regime, but the complementary linear results for Poiseuille flow (Fig. 7c-d) show clearly that this is simply because we have characterized the pen-

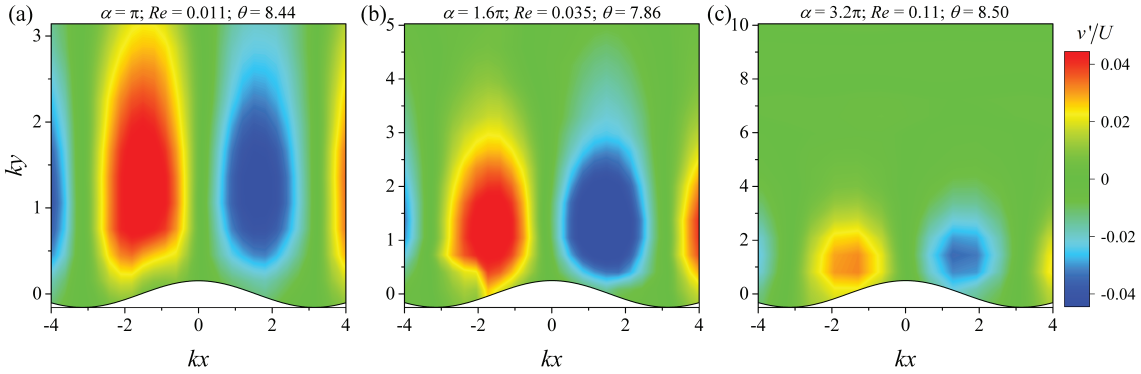

FIG. 8. Detail of the deep viscous flow regime ($\alpha > \pi$, $\theta > 1$) as observed in three devices under conditions of similar θ. (a) Device 3 ($\alpha = \pi$) at $\theta = 8.44$. (b) Device 4 ($\alpha = 1.6\pi$) at $\theta = 7.86$. (c) Device 5 ($\alpha = 3.2\pi$) at $\theta = 8.50$. Flow is from left to right.

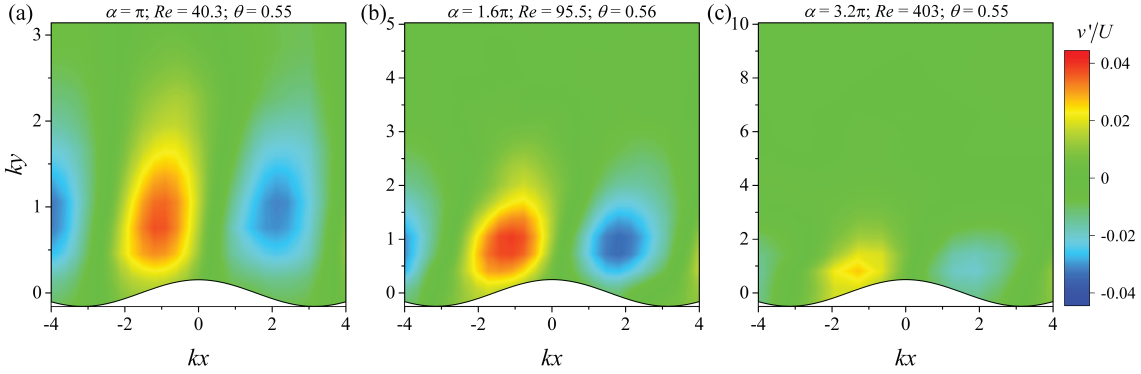

FIG. 9. Detail of the inviscid flow regime ($\alpha > \theta$, $\theta < 1$) as observed in three deep devices under conditions of similar θ. (a) Device 3 ($\alpha = \pi$) at $\theta = 0.55$. (b) Device 4 ($\alpha = 1.6\pi$) at $\theta = 0.56$. (c) Device 5 ($\alpha = 3.2\pi$) at $\theta = 0.55$. Flow is from left to right.

etration using v' as opposed to ${\omega_z}'$. The measures of penetration from linear theory show that $\mathcal{P}_\omega$ (Eq. 7) yields a penetration depth proportional to θ, which emerges from a balance between advection and diffusion. Conversely, the measure of $\mathcal{P}_v$ (Eq. 5) quantifies the penetration of the larger-scale potential flow driven by the wall vorticity, which is the solution to $\nabla^2\psi = -\omega$.

Fig. 8, provides additional experimental details on the appearance of v' perturbations in the deep viscous flow regime in channels of various $\alpha \geq \pi$ at roughly equivalent $\theta \approx 8$. It can be seen that in these deep channels, at each value of α, the perturbation extends a distance $ky \approx \pi$ into the channel. The value π arises as a simple consequence of the generation of two vorticity rolls per wave on the rough surface.

Fig. 9 illustrates the appearance of the v' perturbations observed in experiments performed within the inviscid regime ($\alpha > \theta$, $\theta \lesssim 1$) in the three deep channels ($\alpha \geq \pi$), here all at a similar value of $\theta \approx 0.55$. A one-to-one comparison between the images in Fig. 8a-c and those in Fig. 9a-c, respectively, shows that as the flow transitions from the viscous to the inviscid regime the perturbation is modified in a similar way in each of the three deep channels. In the inviscid regime the perturbations lean forward under the action of shear and penetrate less deeply into the channel as compared with the deep viscous regime. In addition there is a noticable reduction in the intensity of the perturbation (note the color scale is maintained constant between Figs. 8 and 9).

One particular difference between our results and those of Charru and Hinch [2] is that from the measurement of $\mathcal{P}_v$ (see Fig. 7) we are unable to observe the inviscid regime within shallow channels (at least within the range of θ that we could access experimentally). However, some indication of the inviscid regime in the shallow channels is evident in the v' perturbation fields, as shown in Fig. 10. Here it is apparent that as θ is decreased within the inviscid regime in a shallow channel ($\alpha = 0.32\pi$), the perturbation is pushed forward by the shear and also reduced in intensity, just as is observed in the inviscid regime in deeper channels (see Fig. 9). However, in the shallow channels the perturbation continues to reach all the way through the flow domain even for

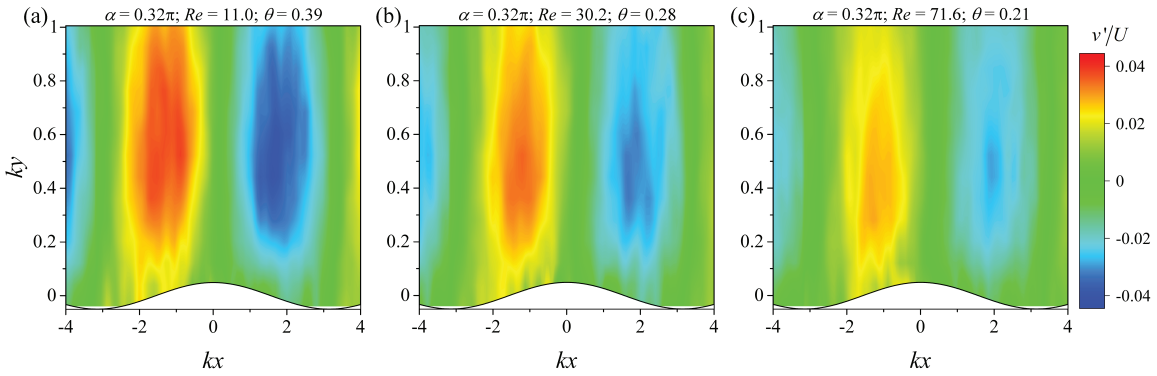

FIG. 10. v' perturbations in a shallow channel (Device 2, $\alpha = 0.32\pi$) under conditions corresponding to the inviscid regime ($\alpha > \theta$, $\theta < 1$). (a) $\theta = 0.39$, (b) $\theta = 0.28$, (c) $\theta = 0.21$. Flow is from left to right.

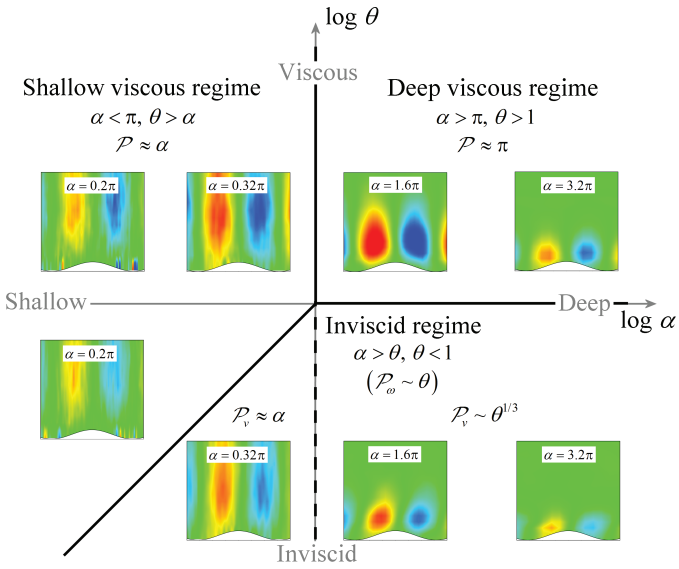

FIG. 11. 'Phase diagram' for Newtonian regimes observed in Poiseuille flow through channels with one wavy surface.

very low $\theta = 0.21$ (Fig. 10c), so that the inviscid regime in such shallow channels is not evident in the measurement of $\mathcal{P}_v$.

Based on the observations and measurements made for Poisseuille flows of Newtonian fluids through channels with wavy surfaces, a 'phase diagram' (of similar form to those presented by Charru and Hinch [2] and Page and Zaki [4]) can be constructed to delineate the regimes of deep viscous, shallow viscous and inviscid flow in $\alpha - \theta$ parameter space. According to our observations, we consider shallow channels as those with $\alpha < \pi$ and deep channels as those with $\alpha > \pi$. The deep viscous regime occupies the top-right quadrant of the phase diagram with $\alpha > \pi$, $\theta \gtrsim 1$ in which, according to both our measures of the penetration depth (Eqs. 5 and 7), $\mathcal{P} \approx \pi$. The shallow viscous regime to the left of the phase diagram is defined by $\alpha < \pi$, $\theta \gtrsim \alpha$, and in this regime we find $\mathcal{P} \approx \alpha$ according to both our measures of the penetration depth (Eqs. 5 and 7). Both the shallow viscous and the deep viscous regimes observed in wavy channel Poisseuille flow are almost exactly equivalent to the regimes predicted by Charru and Hinch and modeled by Page and Zaki for plane Couette flow over a wavy surface [2, 4]. The main differences between our experimental results and their theory arise in the inviscid regime. In our case, the inviscid regime occupies the lower region of the phase diagram defined by $\alpha \gtrsim \theta$, $\theta \lesssim 1$ (as it is in the work of Charru and Hinch [2]), however here we subdivide the inviscid regime into shallow inviscid ($\alpha < \pi$, $\theta \lesssim \alpha$) and deep inviscid ($\alpha > \pi$, $\theta \lesssim 1$) parts. Shallow inviscid behavior is characterized by a distortion of the perturbation but is indistinguishable from the shallow viscous regime in terms of the penetration depth measurement, with $\mathcal{P}_v \approx \alpha$. In the deep inviscid subregime, according to our experimental measure of the penetration depth and linear theory $\mathcal{P}_v \sim \theta^{1/3}$. Linear theory confirms this scaling using the same measure of penetration (Eqs. 5), however linear results also indicate that the associated penetration of the vorticity perturbation in the inviscid regime (for deep and shallow channels) scales as $\mathcal{P}_\omega \sim \theta$, which is in agreement with earlier predictions [2].

VI. SUMMARY AND CONCLUSIONS

In this work we have employed a novel microfabrication technique known as selective laser-induced etching (SLE) to produce a series of five 3D-printed glass channels. Each rectangular channel incorporates one sinusoidal wavy surface of small amplitude and a particular, well-defined wavelength. We have performed spatially-resolved μ-PIV in the channels using two Newtonian fluids of contrasting viscosity in order to measure velocity field perturbations caused to the Poisseuille base flow state by the wavy surface as the imposed flow rate is var-

ied over a wide range. The small amplitude of the wavy surface results in very small perturbations to the transverse velocity components of at most around 5% of the average flow velocity, however these small vector components are accurately measured by the μ-PIV. The SLE technique is shown to be sufficiently precise to enable the fabrication of channels with accurate geometrical parameters that conform to the requirements of linearity, as confirmed by the excellent agreement between our experimental measurements and numerical results from the linear perturbation equations. Our combination of techniques has enabled the first experimental test of the validity of the theoretical predictions and phase diagram made by Charru and Hinch [2] for shear flow over a wavy surface. While their asymptotic analysis assumed a plane Couette base state, here the flow configuration is pressure-driven Poisseuille flow. In general, our results agree remarkably well with theirs and fit into an analogous phase diagram, with only minor modifications which we attribute to the absence of a rigid boundary at the location $ky = \alpha$ ($y = d$) in the case of the Poisseuille flow studied here. The results presented here lay a solid groundwork for benchmark comparison against flows under conditions of more complex geometrical and/or rheological parameters. In particular, we have an interest in viscoelastic shear flows over wavy surfaces, which have recently been studied theoretically by Page and Zaki [4], with the prediction of some intriguing non-local vorticity amplification effects that remain to be confirmed experimentally.

Acknowlegdements. SJH and AQS gratefully acknowledge the support of the Okinawa Institute of Science and Technology Graduate University (OIST) with subsidy funding from the Cabinet Office, Government of Japan. Mr. Alexander Unterkreuter and Mr. Kazumi Toda-Peters from OIST are thanked for their help with the fabrication of devices using the LightFab 3D printer. SJH is very grateful to TA Instruments for the donation of a DHR3 rheometer under their Distinguished Young Rheologist Award scheme.

[1] P. Laure, H. Le Meur, Y. Demay, J. C. Saut, and S. Scotto, J. Non-Newtonian Fluid Mech. **71**, 1 (1997).
[2] F. Charru and E. J. Hinch, J. Fluid Mech. **414**, 195 (2000).
[3] T. A. Zaki and S. Saha, J. Fluid Mech. **626**, 111 (2009).
[4] J. Page and T. A. Zaki, J. Fluid Mech. **801**, 392 (2016).
[5] M. K. S. Verma and V. Kumaran, J. Fluid Mech. **727**, 407 (2013).
[6] V. Kumaran and P. Bandaru, Chem. Eng. Sci. **149**, 156 (2016).
[7] F. Charru, B. Andreotti, and P. Claudin, Annu. Rev. Fluid Mech. **45**, 469 (2013).
[8] P. Luchini and F. Charru, Phys. Rev. Fluids **2**, 012601 (2017).
[9] J. C. Burns and T. Parkes, J. Fluid Mech. **29**, 731 (1967).
[10] I. J. Sobey, J. Fluid Mech. **96**, 1 (1980).
[11] G. Meineke, M. Hermans, J. Klos, A. Lenenbach, and R. Noll, Lab Chip **16**, 820 (2016).
[12] P. Gonzalez-Tello, F. Camacho, and G. Blazquez, J. Chem. Eng. Data (1994).
[13] P. Dontula, C. W. Macosko, and L. Scriven, AIChE J. **44**, 1247 (1998).
[14] C. D. Meinhart, S. T. Wereley, and M. H. B. Gray, Meas. Sci. Technol. **11**, 809 (2000).